Parameter Scans Using a Theory-based Transport Model

Jon E. Kinsey
Lehigh University

in collaboration with

Glenn Bateman
Princeton Plasma Physics Laboratory

Jan Weiland
Chalmers University, Sweden

Presented at the
Thirty-Seventh Annual Meeting
APS Division of Plasma Physics
Louisville, Kentucky
November 6–10, 1995

Abstract

Systematic comparisons are made between TFTR experimental data and theoretical predictions using a theory-based transport model. The transport model includes the Weiland theory for the trapped electron and ion temperature gradient modes[1] and the Guzdar-Drake theory for the resistive ballooning mode[2] and has been successfully benchmarked against over fifty tokamak discharges from seven different tokamaks[3]. Results are presented for a TFTR neutral beam heated gyro-radius scan and also for scans in beta, collisionality, plasma current, density, and heating power. In simulations of the TFTR gyro-radius scan, it is found that changes in the heating profile and resulting small changes in the temperature gradients cause a fundamentally gyro-Bohm model to produce close to Bohm scaling. Simulations of the DIII-D and JET gyro-radius experiments are included.

---

[1] G. Bateman, *et al.*, Phys. Scripta **51**, 597 (1995).

[2] P. N. Guzdar, *et al.*, Phys. Fluids **B 5**, 3712 (1993).

[3] J. E. Kinsey, *et al.*, Phys. Plasmas **2**, 811 (1995).

Multi-mode Model

- We use a combination of theoretically derived transport models to predict the time evolution of temperature and density profiles in tokamaks
  - Weiland model for ITG and TEM modes
  - Guzdar-Drake resistive ballooning modes
  - Rewoldt-Tang-Singer kinetic ballooning modes
  - Kwon-Biglari-Diamond neoclassical MHD mode ($\vec{E} \times \vec{B}$ only)

- Simulated temperature and density profiles match data well for a wide variety of scans using a purely gyro-Bohm model
  - ρ_* scans from DIII-D, TFTR, and JET
    10 L-mode shots with $0.0037 < \rho_*(0) < 0.0128$
    (ITER $\rho_*(0) \sim 0.0015 - 0.0020$)
  - Current, power, density, ν_*, and β, scans
  - L-mode, H-mode, Ohmic, and supershots (See Bateman, **9P40**)
  - Total of more than 50 discharges from 7 different tokamaks

Weiland Transport Model

- Model derived by linearizing fluid equations and computing
  - eigenvalues (frequency and growth rate)
  - eigenvectors (perturbed densities and temperatures)
- Yields transport due to ITG and TEM in one consistent model
- Predicts quasilinear transport for 4 channels - Electron and ion thermal, hydrogenic particles, and impurites.
- Model includes effects of impurities, finite Larmor radius and unequal electron and ion temperatures
- Dependence of heat flux on temperature, density and density gradient leads to off-diagonal terms which can result in particle and heat pinches in outer region of the plasma
- Finite beta, collisionality, and electromagnetic effects have been implemented and are undergoing testing.

Model Update

- Previous model described at the 1995 TTF workshop has been revised
- Guzdar-Drake drift-resistive ballooning model has replaced the Carreras-Diamond resistive ballooning model to provide the correct current scaling.
  - Guzdar-Drake diffusivity:
    $$D^{\mathrm{RB}} = \chi^{\mathrm{RB}} = 0.15(2\pi q_a^2)\rho_e^2 \nu_{\mathrm{ei}} \frac{R_o}{L_p}$$
  - Does not yet include any electromagnetic or diamagnetic effects
  - Channels of transport not separated ($D^{\mathrm{RB}} = \chi_e^{\mathrm{RB}} = \chi_i^{\mathrm{RB}}$)
  - Follows gyro-Bohm scaling, $\chi^{\mathrm{RB}} \sim B_T^{-1}$
- Stochastic field (magnetic flutter) transport has been eliminated. Model is now purely gyro-Bohm ($\chi \sim B_T^{-1}$)
- Kinetic ballooning model has been empirically calibrated against DIII-D and TFTR experimental data.
- Theories used as given (uncalibrated) with exception of kinetic ballooning model

Simulation Methodology

- Experimental data used to prescribe:
  - Boundary conditions for n_e, T_e, T_i (set at x=0.98)
  - Sawteeth events - from soft x-ray (DIII-D and TFTR) and/or time evolution of central electron temperature (JET)
  - Density monitor used to prescribe $\bar{n}_e$
  - Time evolution of Z_{eff} obtained by prescribing edge carbon impurity level and influxing impurities to match experimental $\bar{Z}_{\text{eff}}$

- Simulations initialized in the Ohmic phase ($>$ 3–4 τ_E's prior to NBI)

- Systematic statistical techniques have been developed to calibrate and test models against experimental data (see Phys. Plasmas **2**, 811 (1995))

- We predict the impurity and hydrogenic density profiles along with electron and ion temperature profiles

- ITER simulations ignite with peaked density profile <u>and</u> density ramp using 40MW of NBI

Neutral Beam Heated DIII-D and TFTR ρ_* Scans

Major Plasma Parameters for NBI Discharges

Tokamak	DIII-D	DIII-D	TFTR	TFTR	TFTR	TFTR
Shot	78283	78109	50921	50904	50911	52504
Type	High ρ_*	Low ρ_*	High ρ_*	Med ρ_*	Low ρ_*	Low ρ_*
R_o (m)	1.69	1.64	2.45	2.45	2.45	2.45
a (m)	.618	.624	.797	.798	.798	.799
κ_a	1.86	1.85	1.00	1.00	1.00	1.00
δ_a	0.60	0.60	0.00	0.00	0.00	0.00
B_T (T)	1.00	2.00	2.14	2.86	4.23	4.76
I_p (MA)	.465	.992	.890	1.19	1.78	1.98
$\bar{n}_e(10^{19}/m^3)$	1.20	2.74	1.77	2.66	4.37	5.17
$\bar{Z}_{\text{eff}}$	2.45	1.40	2.38	2.10	1.79	2.34
$\rho_*(0)$ (m)	.0128	.0082	.0065	.0054	.0041	.0037
P_{aux} (MW)	0.51	2.00	4.66	7.31	17.72	22.67
τ_E^{th}(secs)	0.074	0.093	0.072	0.087	0.073	0.083
W_{th} (MJ)	0.043	0.178	0.158	0.276	0.918	0.825
τ_{saw}^{OH}(secs)	.0173	.026	.050	.050	.050	.032
τ_{saw}^{L}(secs)	.0297	.079	.118	.165	.163	.180
t_{saw}^{*}(secs)	3.87	3.86	3.88	3.87	3.80	3.89
Diagnostic Time (secs)	3.90	3.90	3.95	3.95	3.93	3.93

From soft x-ray and/or evolution of central temperature:

τ_{saw}^{OH} Sawtooth period during Ohmic phase

τ_{saw}^{NB} Sawtooth period during neutral beam phase

t_{saw}^{*} Time of last sawtooth prior to diagnostic time

Radiofrequency Heated DIII-D and JET ρ_* Scans

Major Plasma Parameters for RF Discharges

Tokamak	DIII-D	DIII-D	JET	JET
Shot	78281	78106	27658	27654
Type	High ρ_*	Low ρ_*	High ρ_*	Low ρ_*
R_o (m)	1.70	1.70	2.95	2.94
a (m)	.628	.629	1.18	1.18
κ_a	1.84	1.87	1.44	1.44
δ_a	0.60	0.60	0.30	0.30
B_T (T)	1.00	2.00	1.70	3.47
I_p (MA)	0.52	1.00	2.06	4.00
$\bar{n}_e(10^{19}/m^3)$	1.39	3.78	1.62	3.95
A_H	2.00	2.00	1.93	1.93
$\bar{Z}_{\rm eff}$	2.5	2.1	3.33	3.50
$\rho_*(0)$	.0123	.0076	.0076	.0044
$P_{\rm aux}$ (MW)	0.38	1.5	3.10	10.3
τ_E^{th}(secs)	0.074	0.091		
$W_{\rm th}$ (MJ)	0.044	0.179		
$\tau_{\rm saw}^{OH}$(secs)	.016	.017	.071	.071
$\tau_{\rm saw}^{L}$(secs)	.021	.024	.211	.328
$t_{\rm saw}^{*}$(secs)	2.58	2.53	53.5	51.7
Diagnostic Time (secs)	2.60	2.55	55.0	52.0

From soft x-ray and/or evolution of central temperature:

$\tau_{\rm saw}^{OH}$ Sawtooth period during Ohmic phase

$\tau_{\rm saw}^{NB}$ Sawtooth period during neutral beam phase

$t_{\rm saw}^{*}$ Time of last sawtooth prior to diagnostic time

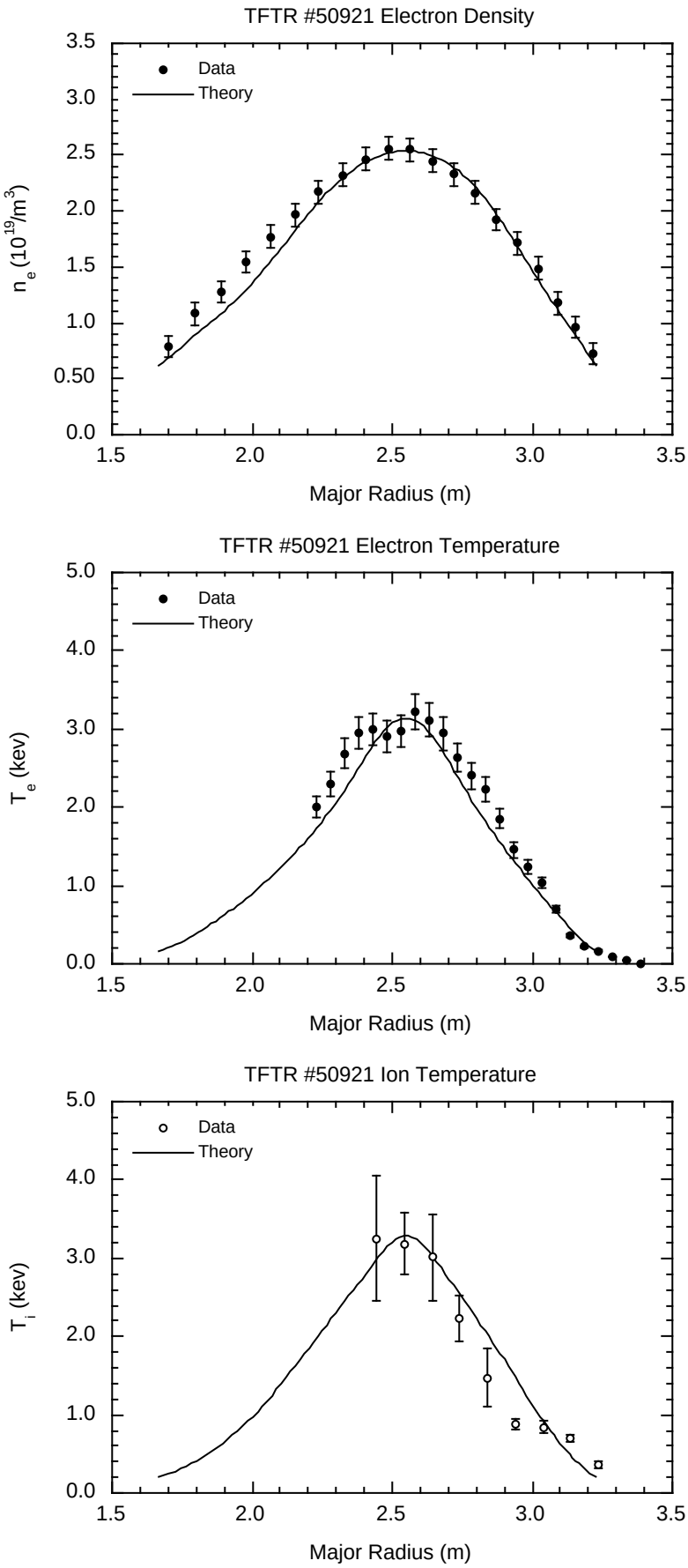

High ρ_*
$\rho_*(0) = 0.0065$

Figure 1. Electron density and temperature profiles for the high ρ_* discharge TFTR #50921 at 3.95 seconds.

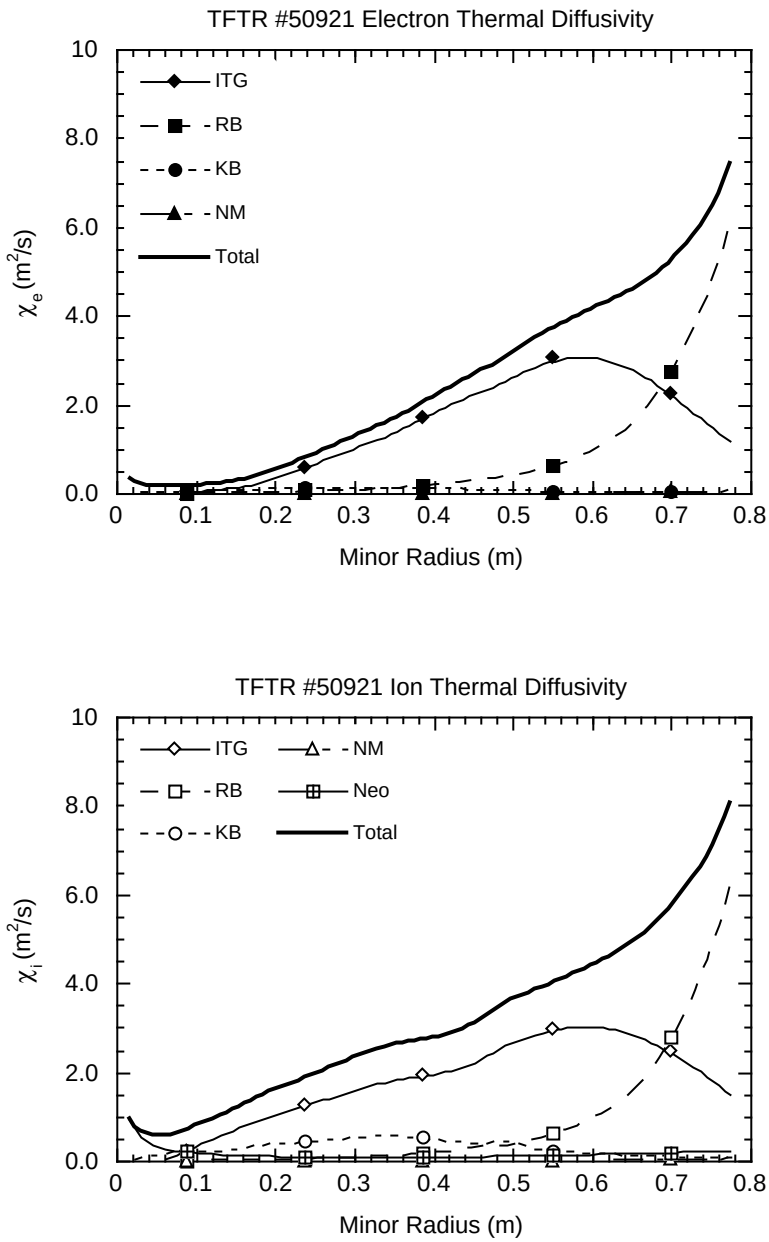

Figure 2. Predicted thermal diffusivities for the high ρ_* discharge TFTR #50921. Here, ITG denotes the drift waves; RB, the resistive ballooning mode; KB, the kinetic ballooning mode; NM, the neoclassical MHD mode;Neo, the neoclassical transport; and $Total$ denotes the total thermal diffusivity.

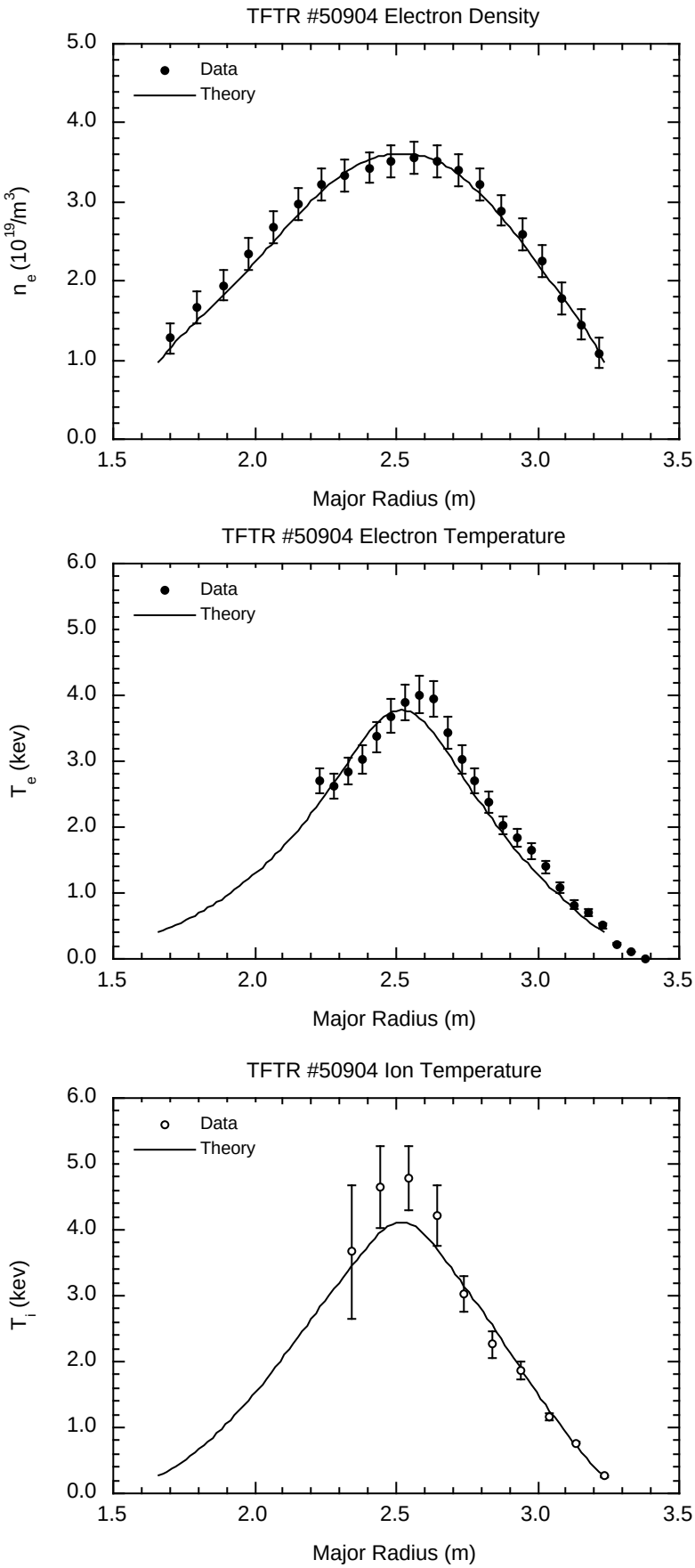

Medium ρ_*
$\rho_*(0) = 0.0054$

Figure 3. Electron density and temperature profiles for the medium ρ_* discharge TFTR #50904 at 3.95 seconds.

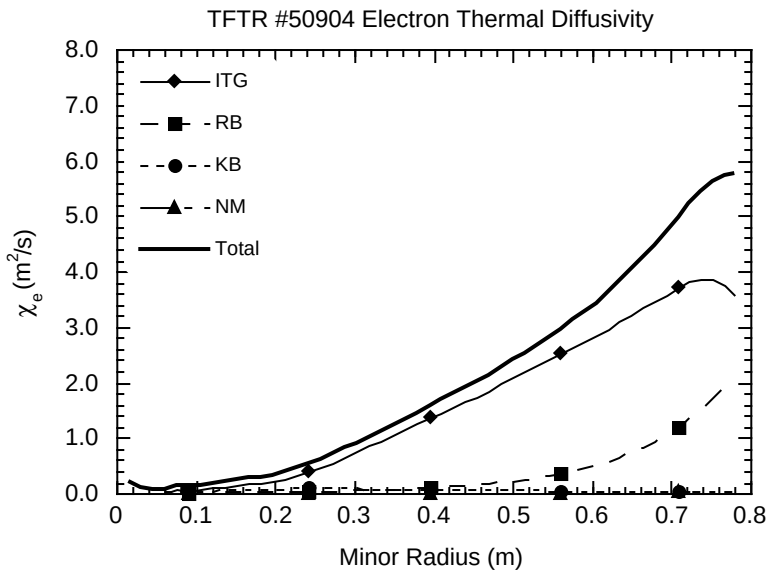

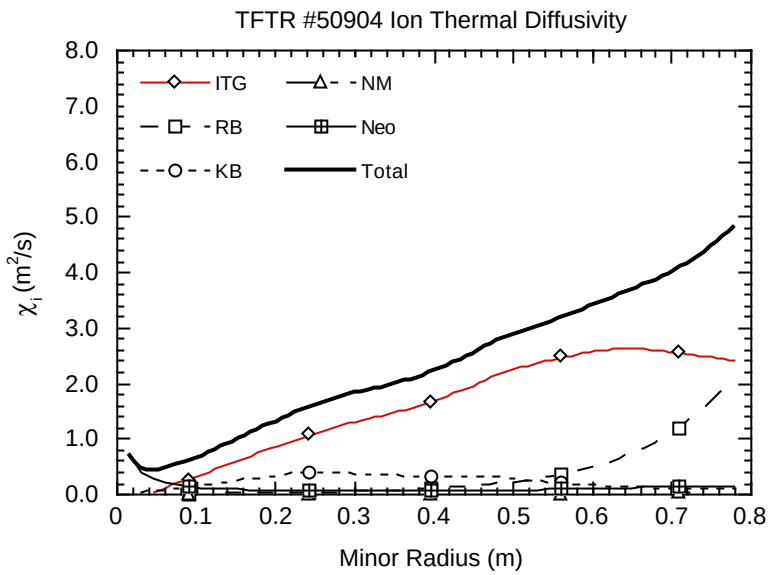

Figure 4. Predicted thermal diffusivities for the medium ρ_* discharge TFTR #50904. Here, ITG denotes the drift waves; RB, the resistive ballooning mode; KB, the kinetic ballooning mode; NM, the neoclassical MHD mode;Neo, the neoclassical transport; and $Total$ denotes the total thermal diffusivity.

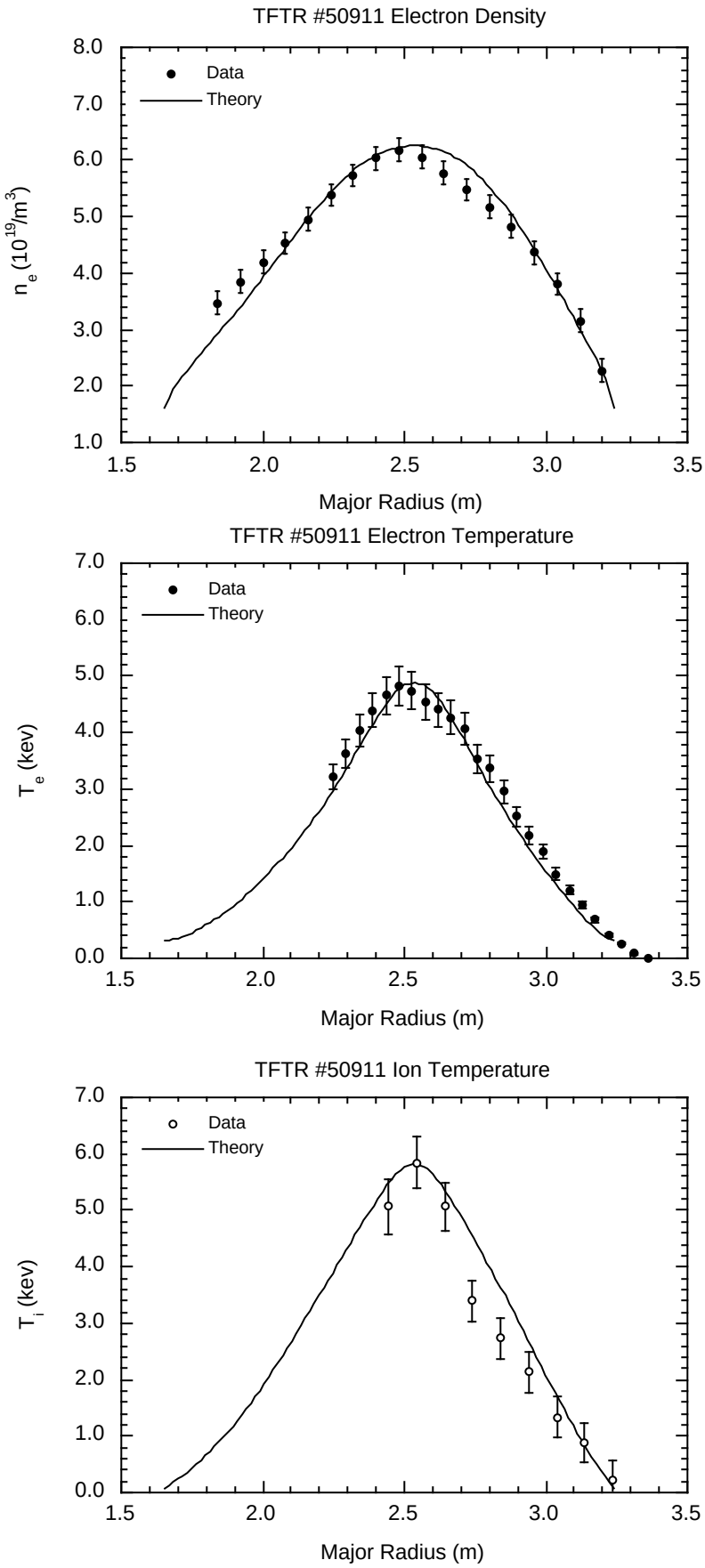

Low ρ_*
$\rho_*(0) = 0.0041$

Figure 5. Electron density and temperature profiles for the low ρ_* discharge TFTR #50911 at 3.93 seconds.

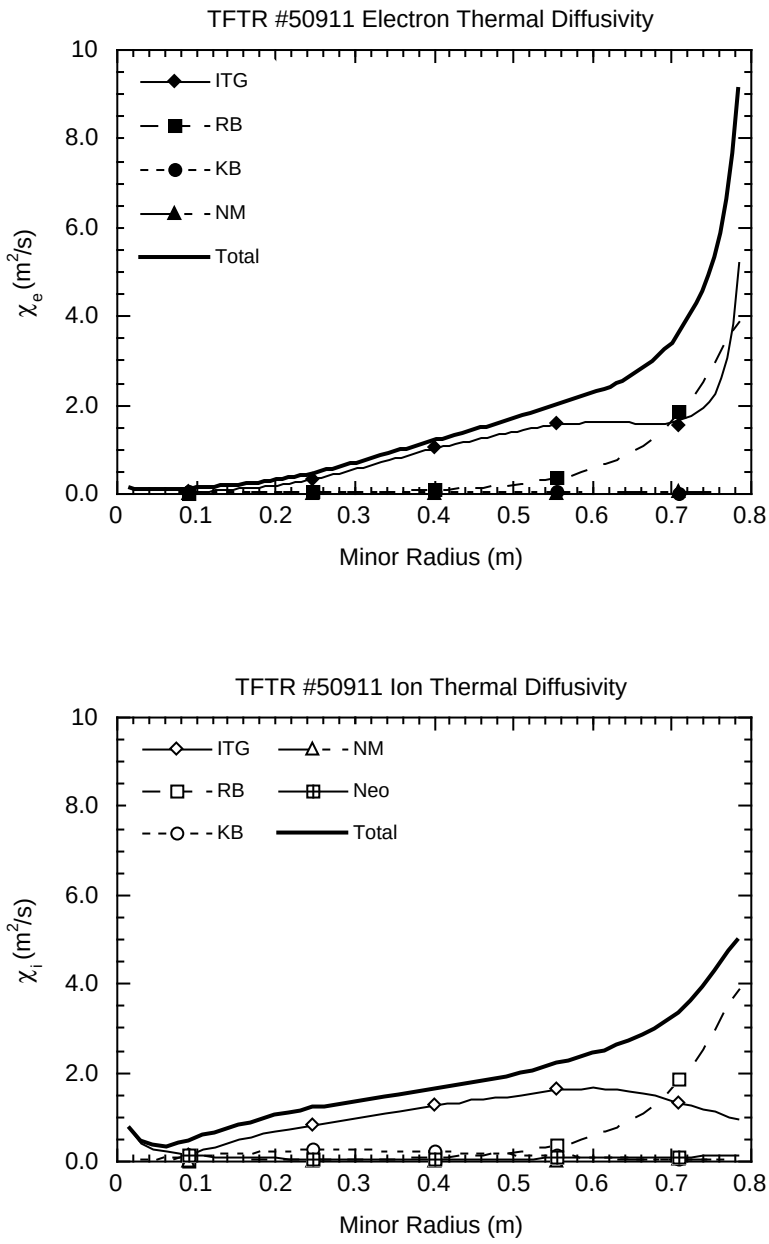

Figure 6. Predicted thermal diffusivities for the low ρ_* discharge TFTR #50911. Here, ITG denotes the drift waves; RB, the resistive ballooning mode; KB, the kinetic ballooning mode; NM, the neoclassical MHD mode;Neo, the neoclassical transport; and $Total$ denotes the total thermal diffusivity.

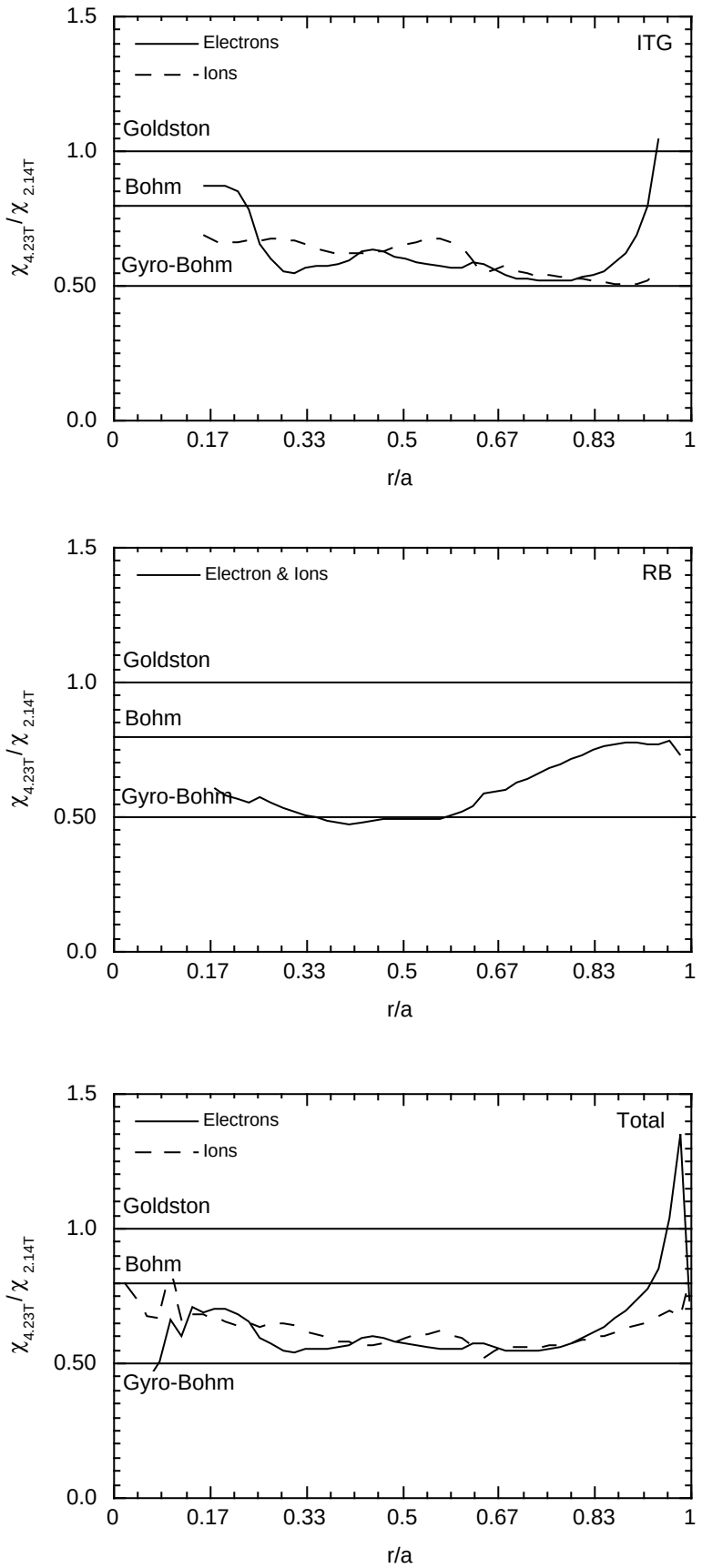

Figure 8. Electron and ion thermal diffusivities ratios (low ρ_* / high ρ_*) versus normalized minor radius for the TFTR ρ_* scan.

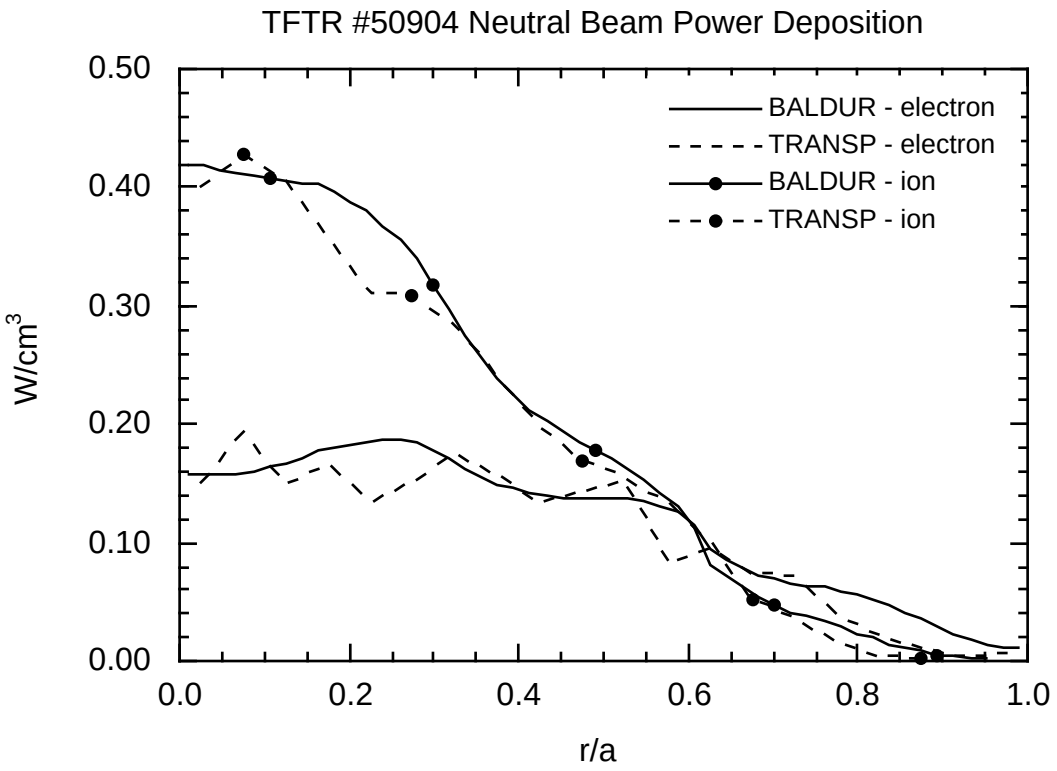

Figure 9. Comparison of the predicted TRANSP and BALDUR neutral beam deposition profiles for the medium ρ_* TFTR shot #50904 at 3.95 seconds.

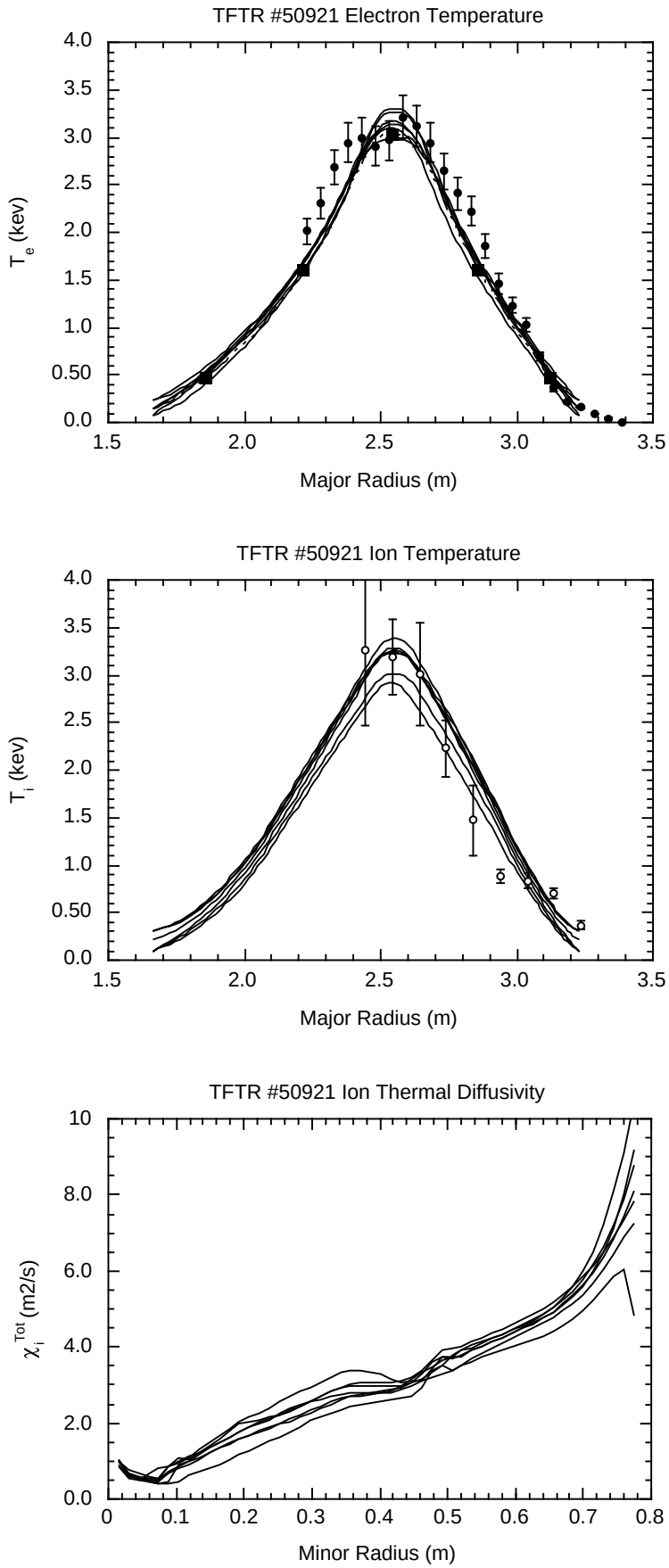

Figure 10. Sensitivity of the temperature profiles and ion thermal diffusivity to the choice of edge boundary temperatures for the high ρ_* TFTR shot #50904 at 3.95 seconds. Here, the boundary electron and ion temperatures were varied independently by as much as 50% from their nominal values.

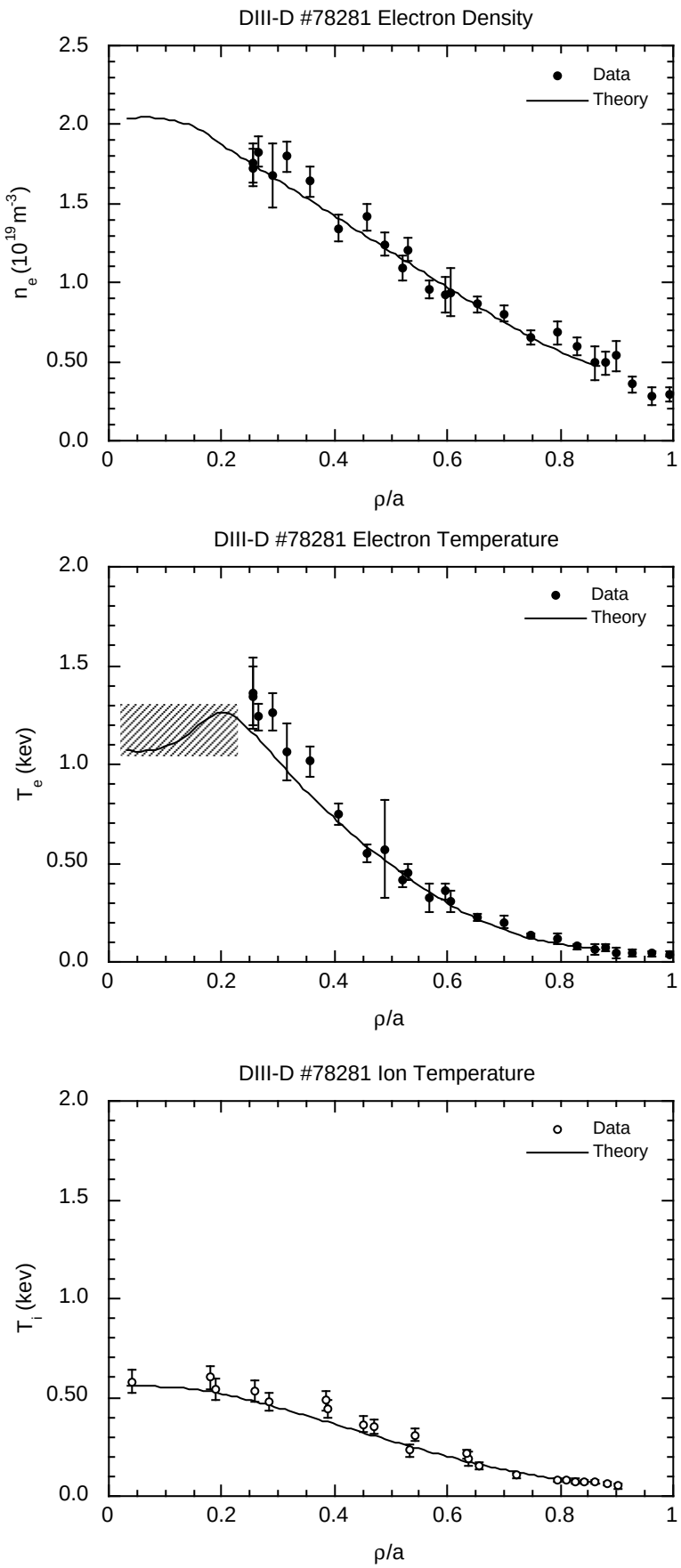

High ρ_*
$\rho_*(0) = 0.0123$

Figure 11. Electron density and temperature profiles for the high ρ_* discharge DIII-D #78281 at 2.60 seconds.

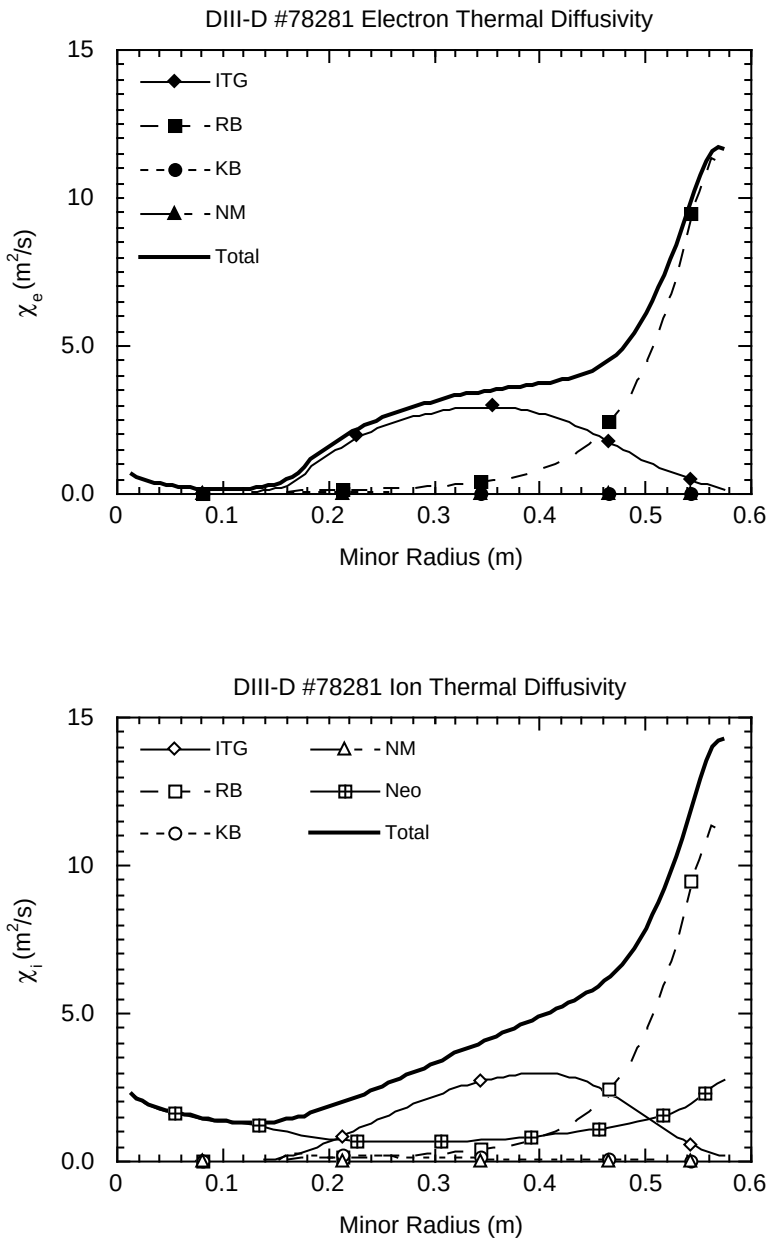

Figure 12. Predicted thermal diffusivities for the high ρ_* discharge DIII-D #78281. Here, ITG denotes the drift waves; RB, the resistive ballooning mode; KB, the kinetic ballooning mode; NM, the neoclassical MHD mode;Neo, the neoclassical transport; and $Total$ denotes the total thermal diffusivity.

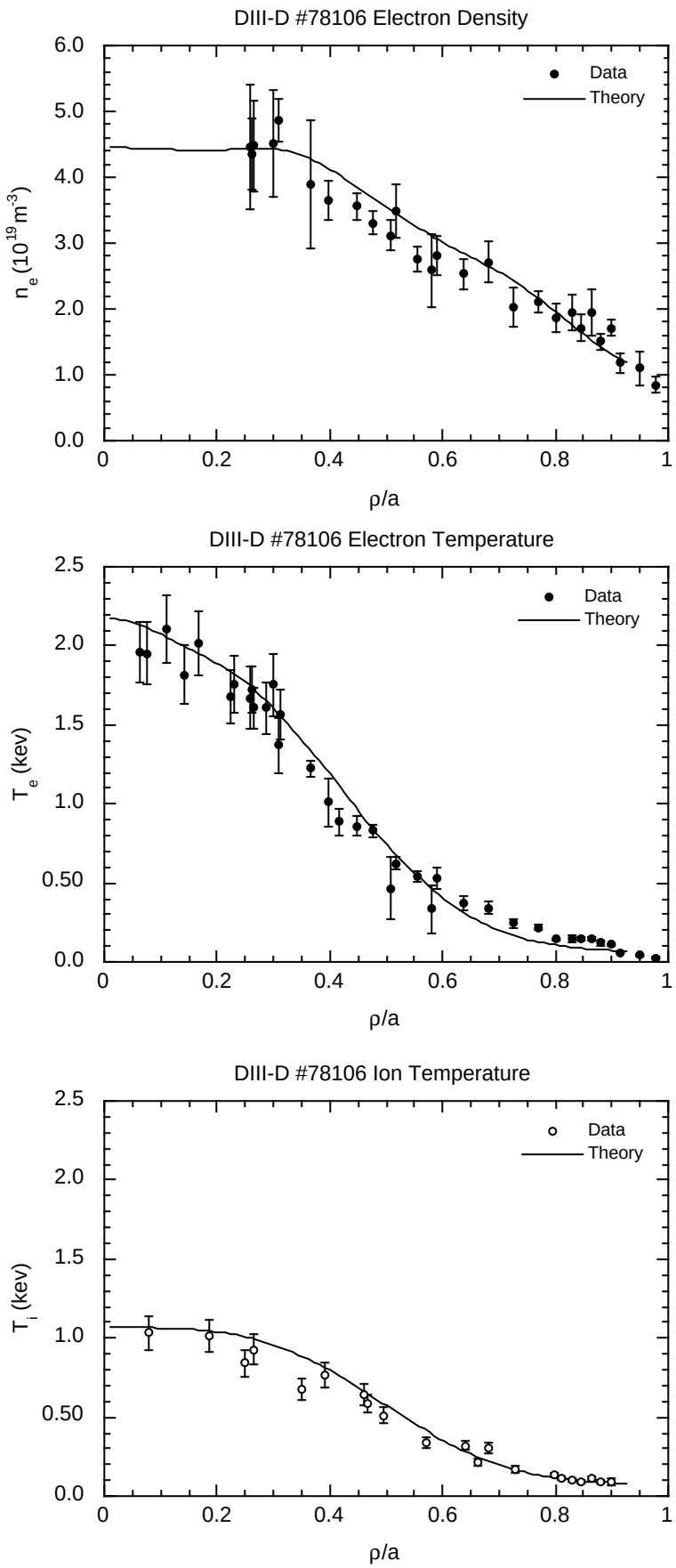

Low ρ_*
$\rho_*(0) = 0.0076$

Figure 13. Electron density and temperature profiles for the low ρ_* discharge DIII-D #78106 at 2.55 seconds.

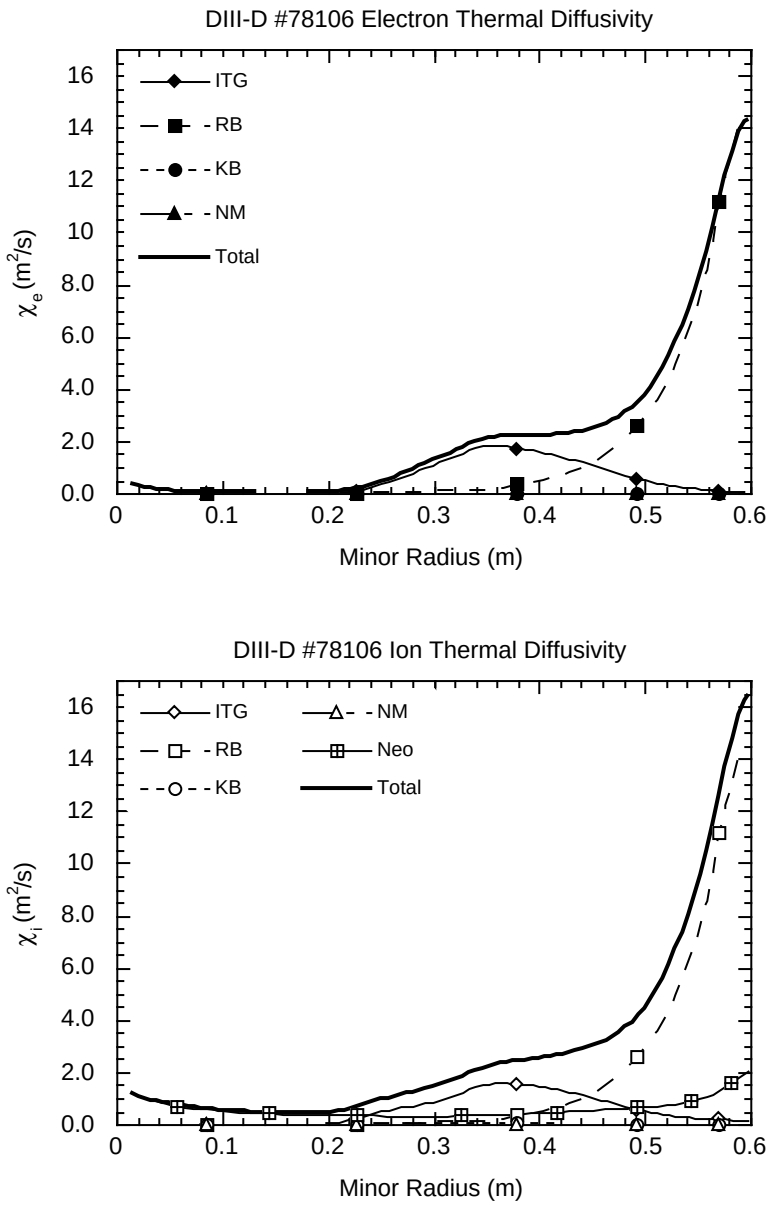

Figure 14. Predicted thermal diffusivities for the low ρ_* discharge DIII-D #78106. Here, ITG denotes the drift waves; RB, the resistive ballooning mode; KB, the kinetic ballooning mode; NM, the neoclassical MHD mode;Neo, the neoclassical transport; and $Total$ denotes the total thermal diffusivity.

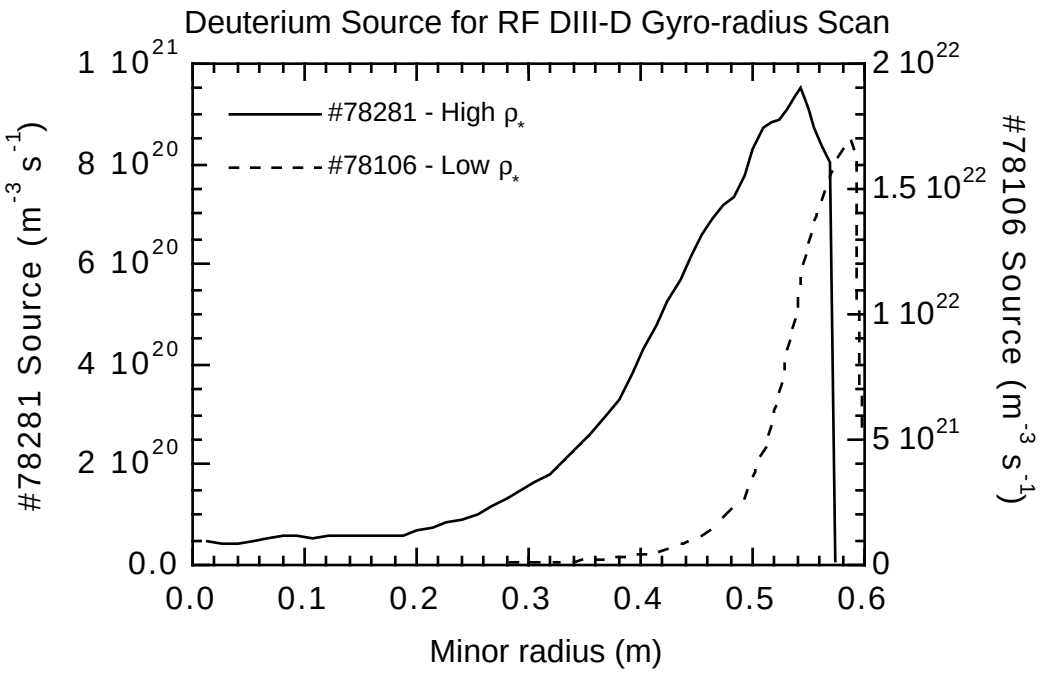

Figure 15. Neutral particle source and collisionality versus minor radius for the high (solid line) and low ρ_* (dashed line) DIII-D RF shots.

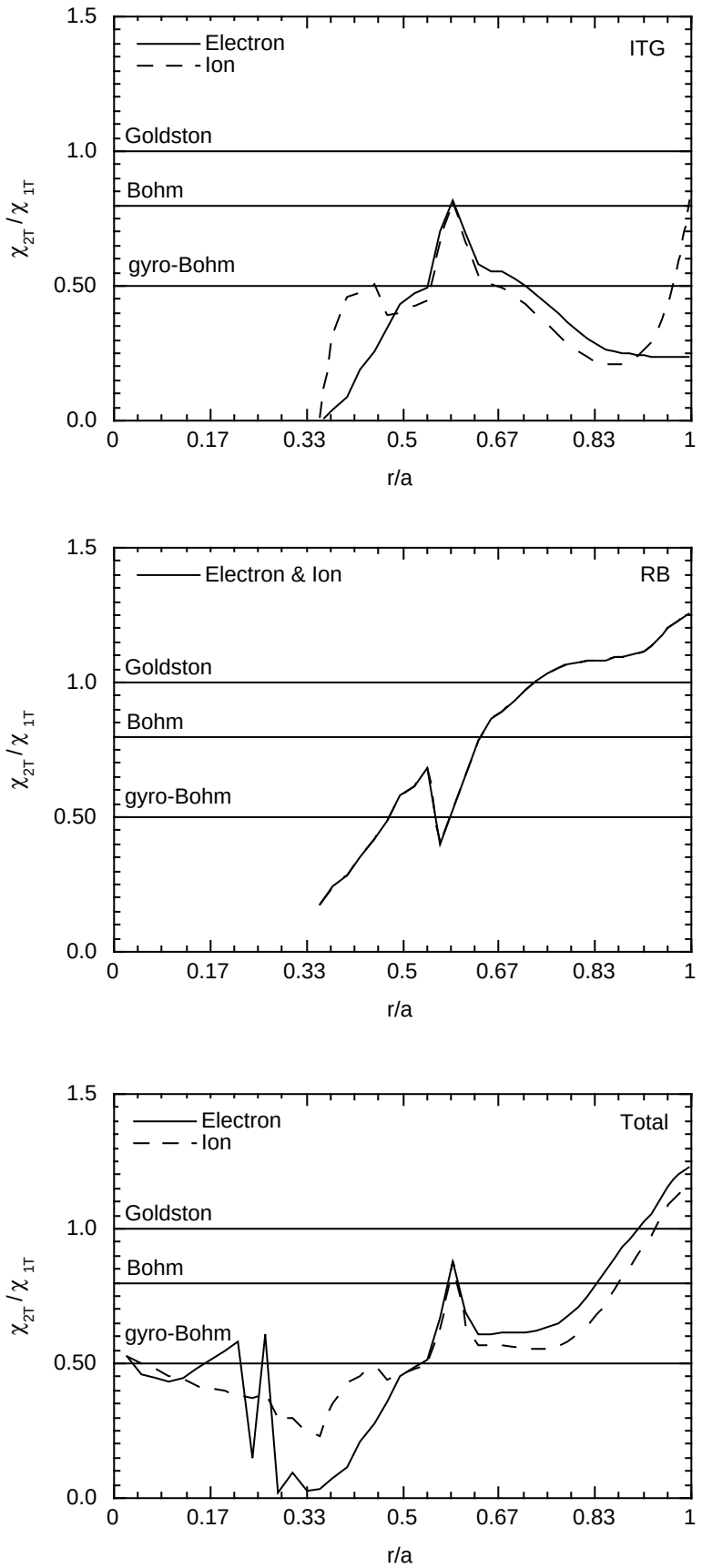

Figure 16. Electron and ion thermal diffusivities ratios (low ρ_* / high ρ_*) versus normalized minor radius for the DIII-D RF ρ_* scan.

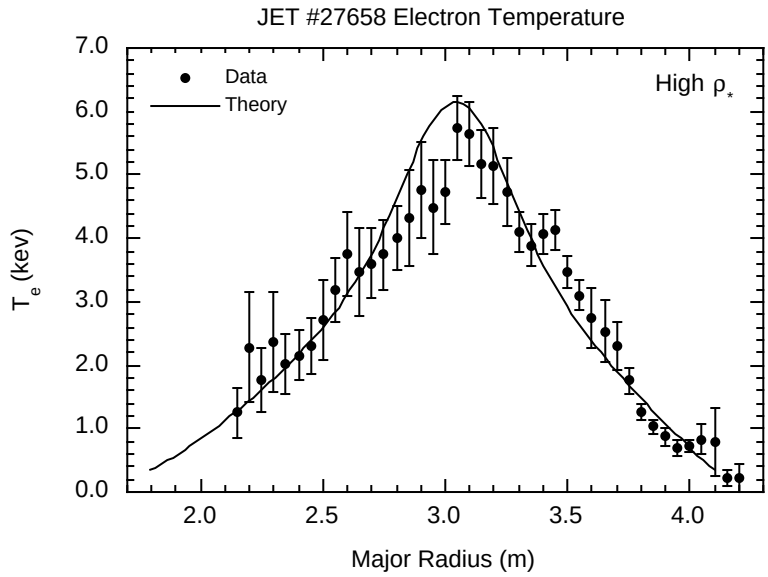

High ρ_*
$\rho_*(0) = 0.0076$

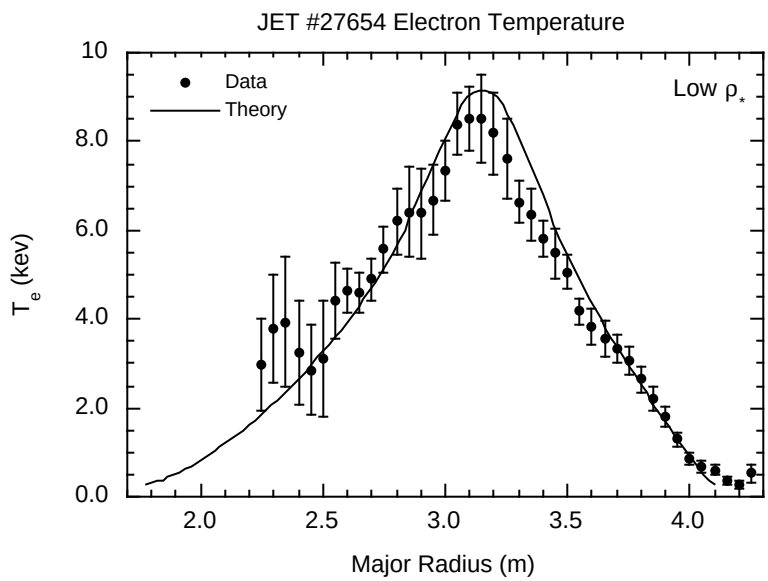

Low ρ_*
$\rho_*(0) = 0.0044$

Figure 17. Electron temperature profiles for the JET high ρ_* discharge #27658 and low ρ_* discharge #27654 at 55.0 and 52.0 seconds, respectively.

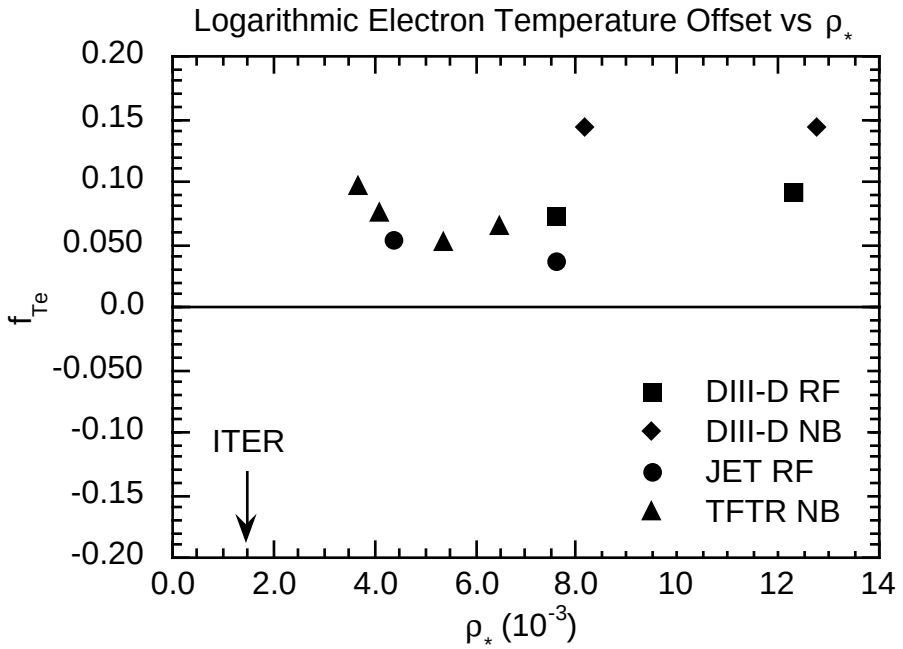

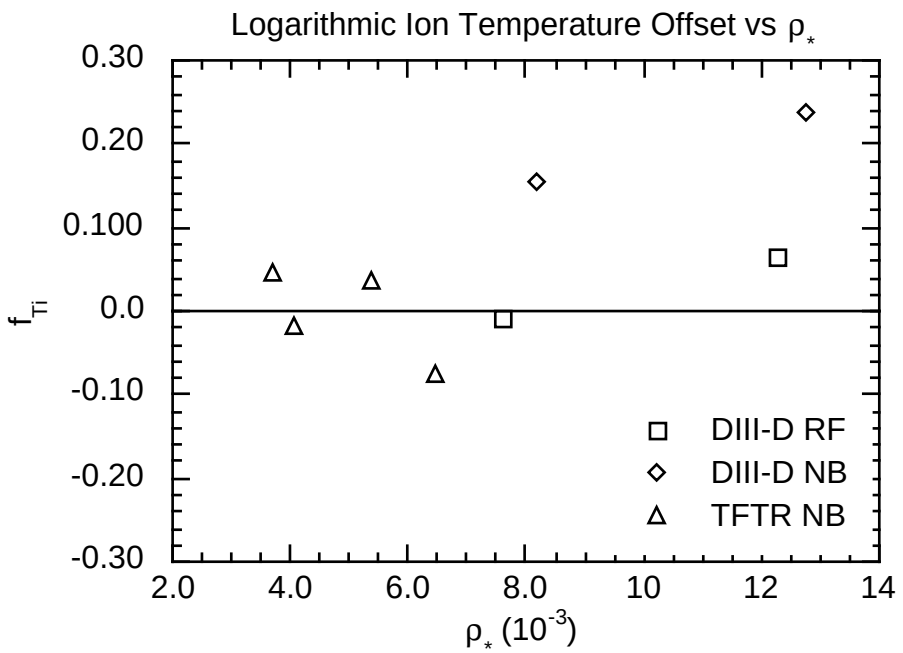

Figure 18. Computed logarithmic offset versus ρ_* for all the DIII-D, JET and TFTR discharges. The squares denote the DIII-D RF shots, the diamonds denote the DIII-D NB shots, the circles denote the JET shots, and the triangles denote the TFTR shots

Neutral Beam Heated TFTR β and ν_* Scans

Major Plasma Parameters

Tokamak Shot	TFTR 52527	TFTR 50903	TFTR 50862	TFTR 64817	TFTR 65012	TFTR 64964	TFTR 64805
Type	High ν_*	Med ν_*	Low ν_*	Low β	Med β	High β	High β
R_o (m)	2.45	2.45	2.45	2.55	2.54	2.54	2.55
a (m)	.796	.797	.797	.894	.893	.893	.897
B_T (T)	2.15	2.86	3.55	3.80	4.07	4.33	4.59
I_p (MA)	0.89	1.19	1.48	1.59	1.70	1.81	1.87
$\bar{n}_e(10^{19}/m^3)$	2.27	2.20	2.48	2.10	2.65	3.30	4.70
$\bar{Z}_{\text{eff}}$	1.94	2.75	3.88	1.53	1.78	1.55	1.70
$\nu_*(0)$ (m)	.0063	.0059	.0053	-	-	-	-
β_p^{dia}	-	-	-	0.20	0.28	0.36	0.53
P_{aux} (MW)	4.35	9.66	12.0	7.31	6.78	13.4	23.5
τ_E^{th}(secs)	0.084	0.072	0.076	0.203	0.127	0.11	0.098
W_{th} (MJ)	0.286	0.447	0.760	0.539	0.768	1.08	1.79
τ_{saw}^{OH}(secs)	.050	.030	.022	.050	.030	.030	.028
τ_{saw}^{L}(secs)	.098	.160	.240	.165	.250	.240	0.0
t_{saw}^{*}(secs)	3.91	3.85	3.81	3.87	3.98	4.02	3.0
Diagnostic Time (secs)	3.93	3.95	3.95	3.83	4.47	4.16	3.97

From soft x-ray and/or evolution of central temperature:

τ_{saw}^{OH} Sawtooth period during Ohmic phase

τ_{saw}^{NB} Sawtooth period during neutral beam phase

t_{saw}^{*} Time of last sawtooth prior to diagnostic time

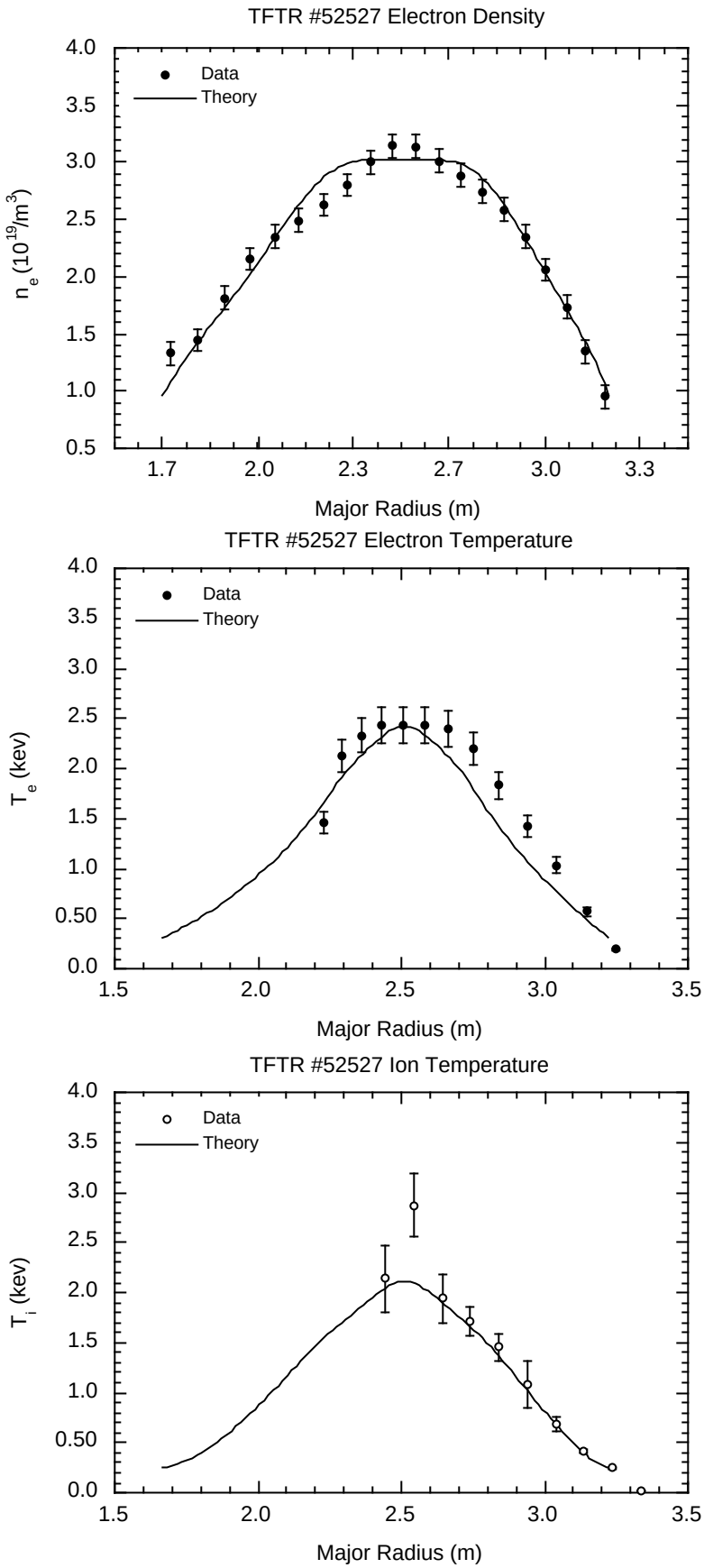

Figure 19. Electron density and temperature profiles for the high ν_* discharge TFTR #52527 at 3.95 seconds.

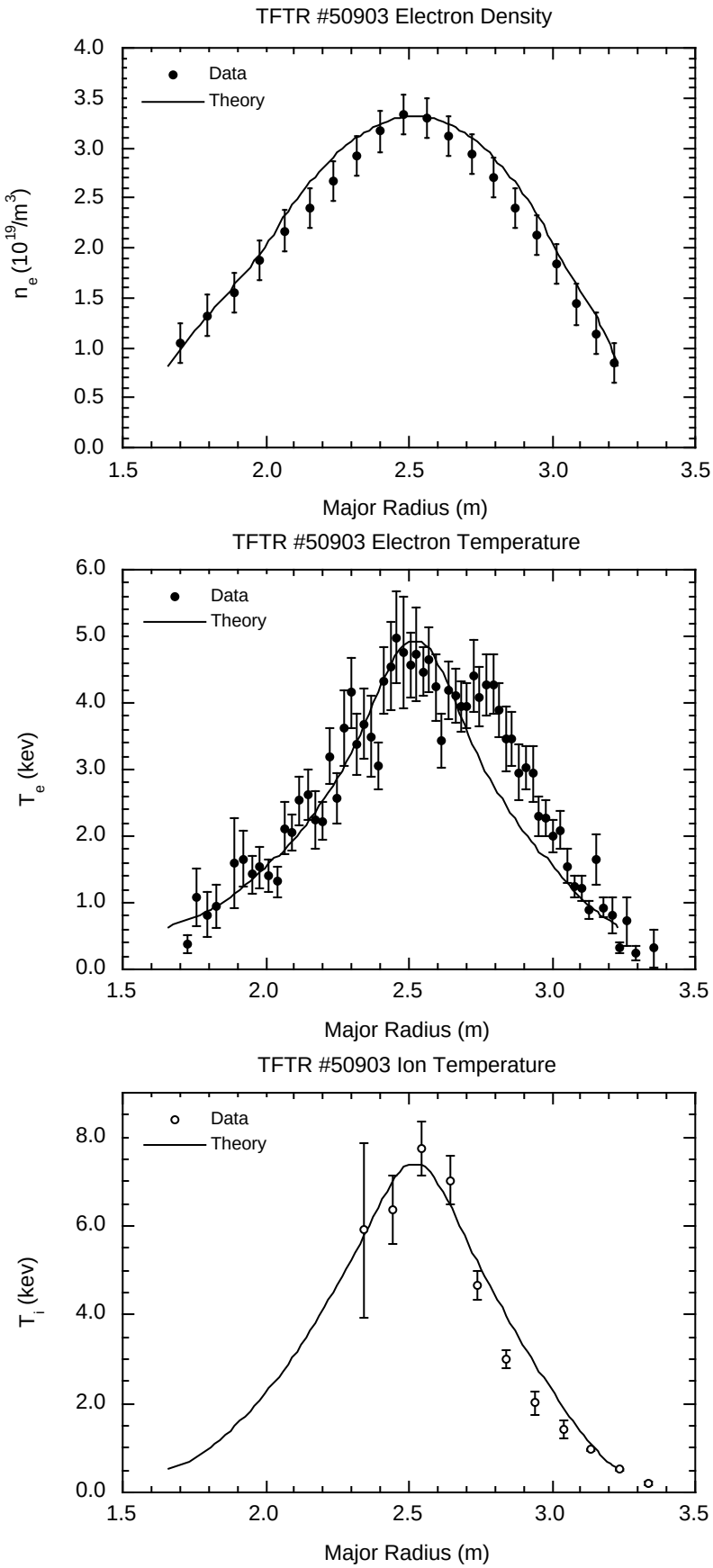

Figure 20. Electron density and temperature profiles for the medium ν_* discharge TFTR #50903 at 3.95 seconds.

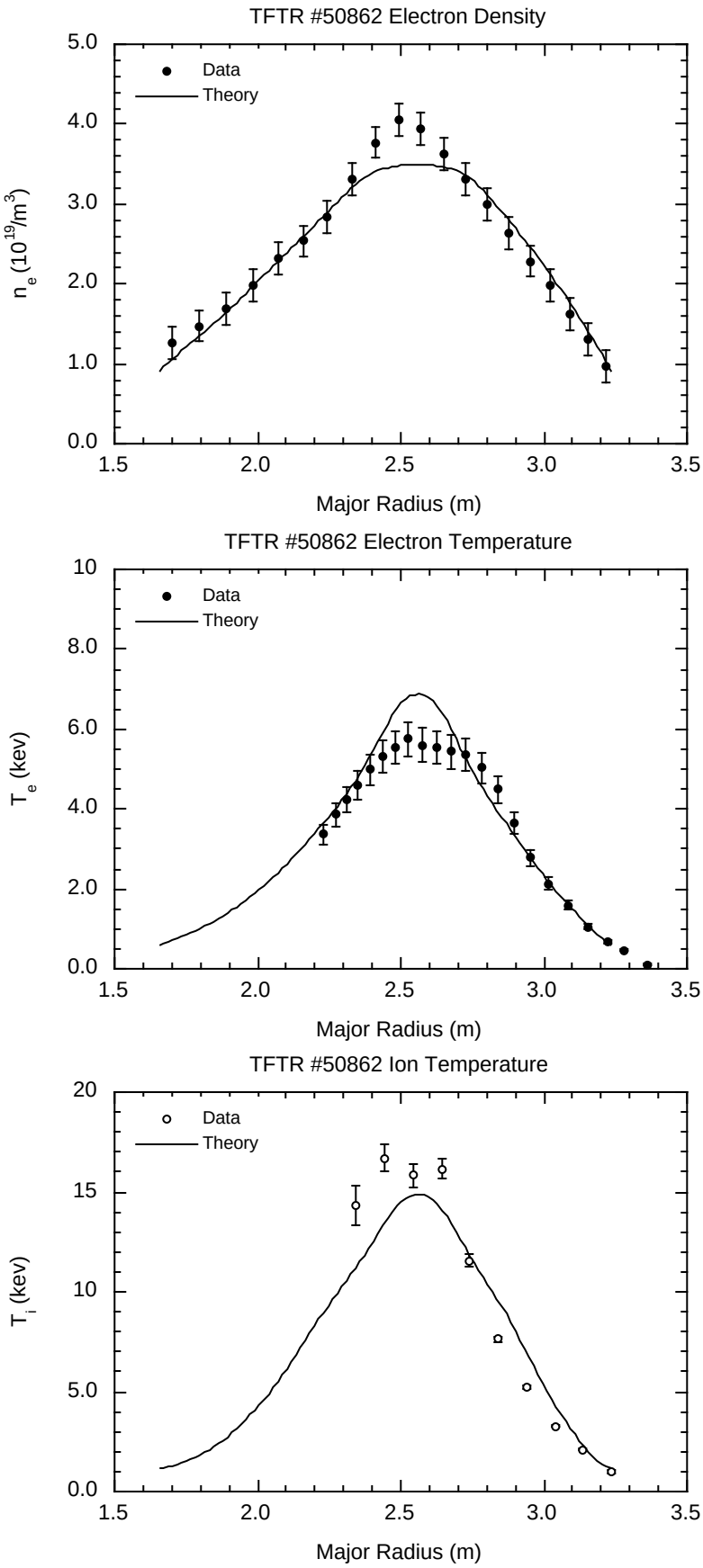

Figure 21. Electron density and temperature profiles for the low ν_* discharge TFTR #50862 at 3.95 seconds.

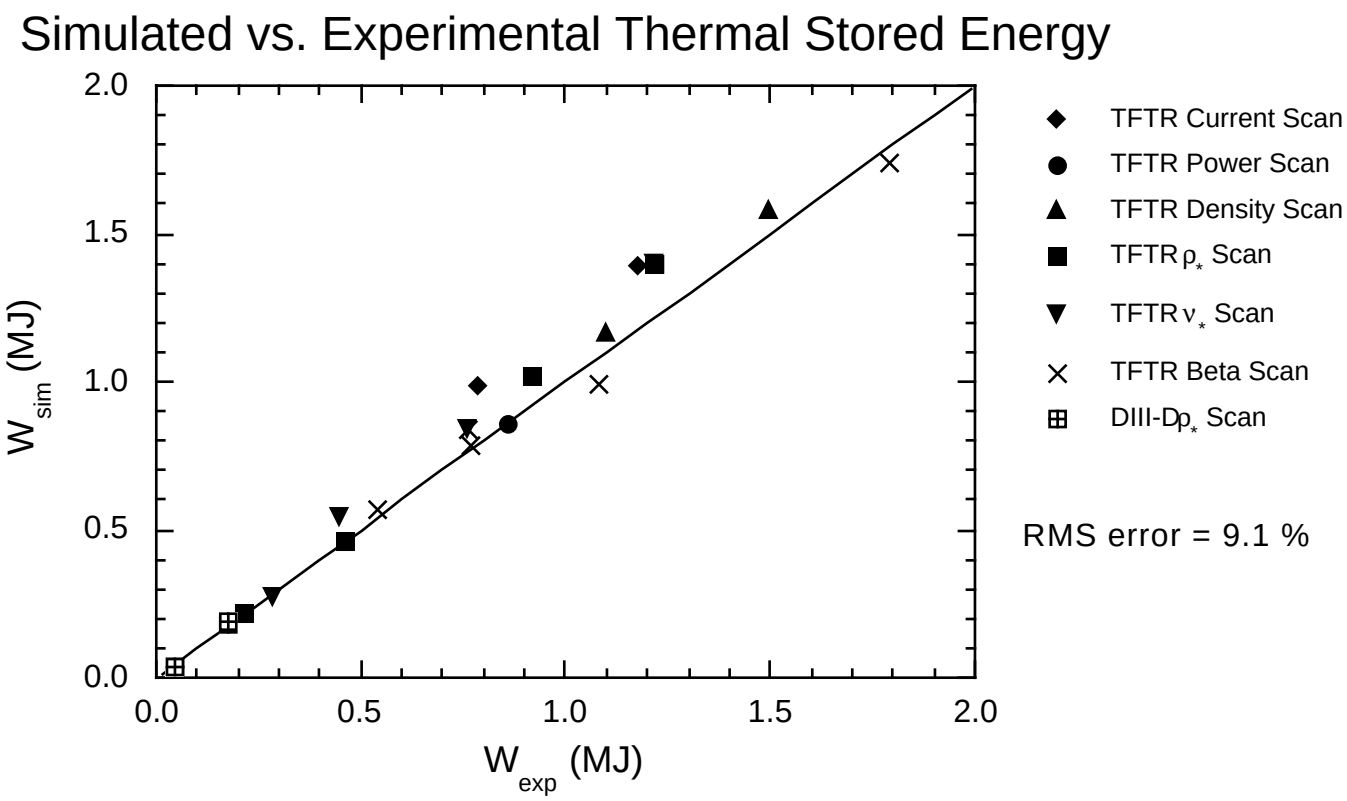

Figure 22. Predicted versus experimental thermal stored energy using for TFTR density, power, current, ρ_*, ν_*, and beta scans at their respective diagnostic times. The DIII-D RF ρ_* scan is also included.